Divergent-beam backprojection-filtration formula with applications to region-of-interest imaging

Aymeric Reshef, Cyril Riddell, Yves Trousset, Saïd Ladjal, Isabelle Bloch

Divergent-beam backprojection-filtration formula with applications to region-of-interest imaging

Aymeric Reshef, Cyril Riddell, Yves Trousset, Saïd Ladjal, and Isabelle Bloch

***Abstract*—We propose a new backprojection-filtration (BPF) method for cone-beam computed tomography (CBCT) with flat-panel detectors over circular orbits. The method is exact in the fan-beam geometry and provides an approximate CBCT reconstruction that is different from the standard Feldkamp-Davis-Kress (FDK) method. More interestingly, it can be used for region-of-interest (ROI) reconstruction by complementing a truncated low-noise acquisition with dense angular sampling by additional non-truncated views that are either high-noise or angularly undersampled.**

I. Introduction

Filtered backprojection (FBP) performs poorly when projections are truncated, unless data extrapolation is performed prior to filtering. Alternative direct reconstruction methods were derived to address the issue of ROI reconstruction [1]. However, when not in parallel-beam geometry, they require a dense angular sampling of the projections.

In the case of interior tomography, it was shown that no unique solution could be obtained from the truncated projections only. However, a tiny additional information, such as a prior knowledge on the image itself [2] or a few additional untruncated measurements [3] is enough to stabilize the problem. Unfortunately, no closed-form analytical solution exists and iterative reconstruction has been used instead.

In this work, we propose a new backprojection-filtration (BPF) formula in cone-beam geometries with flat-panel detectors and circular orbits, which is used to design a direct reconstruction method for ROI imaging. The formula is derived in Section II. The application of the method to ROI imaging is described in Section III. Experiments are presented in Section IV and results are shown in Section V.

II. Method

A. Cone-beam geometry

Let $\Theta = [0, 2\pi]$. For $\theta \in \Theta$, we write $\boldsymbol{\theta} = (\cos\theta, \sin\theta, 0)^T$ and $\boldsymbol{\theta}^\perp = (-\sin\theta, \cos\theta, 0)^T$. The X-ray source is located at point $\boldsymbol{\xi}_\theta = -d\boldsymbol{\theta}$, where d is the source-to-rotation-axis distance. The detector is located at a distance D from the X-ray source. It is a plane orthogonal to the line passing through the center of rotation and the source point $\boldsymbol{\xi}_\theta$. A 3D point $\boldsymbol{x} \in \mathbb{R}^3$ projects onto the detector plane at coordinates $(u_\theta(\boldsymbol{x}), v_\theta(\boldsymbol{x}))$; without loss of generality, we write, for $\alpha \in \Theta$:

$$\boldsymbol{x} = \begin{pmatrix} \boldsymbol{x} \cdot \boldsymbol{\alpha} \\ \boldsymbol{x}_{\alpha^\perp} \end{pmatrix}, \tag{1}$$

where $\boldsymbol{x}_{\alpha^\perp} \in \mathbb{R}^2$ consists of the coordinates of $\boldsymbol{x}$ in the plane of equation $\boldsymbol{x} \cdot \boldsymbol{\alpha} = 0$. When looking only at points $\boldsymbol{x}$ belonging to a plane of equation: $\boldsymbol{x} \cdot \boldsymbol{\alpha} = x_\alpha$, where $x_\alpha \in \mathbb{R}$, the relationship between $(u_\theta(\boldsymbol{x}), v_\theta(\boldsymbol{x}))$ and $\boldsymbol{x}$ is given by:

$$\begin{pmatrix} s_\theta(\boldsymbol{x}) u_\theta(\boldsymbol{x}) \\ s_\theta(\boldsymbol{x}) v_\theta(\boldsymbol{x}) \\ s_\theta(\boldsymbol{x}) \end{pmatrix} = H_\theta^\alpha(x_\alpha) \begin{pmatrix} \boldsymbol{x}_{\alpha^\perp} \\ 1 \end{pmatrix}, \tag{2}$$

where the matrix $H_\theta^\alpha(x_\alpha) \in \mathbb{R}^{3\times 3}$ is a homography matrix.

The cone-beam projection of an image f at angle θ is denoted p_θ. It is defined at each detector coordinate (u, v) as the integral of f along the line joining $\boldsymbol{\xi}_\theta$ to (u, v). The full-scan, cone-beam tomographic acquisition over a circular orbit is the collection $p = \{p_\theta \mid \theta \in \Theta\}$. We define the backprojection from angle θ of a single projection p_θ as: $\mathcal{B}_\theta[p_\theta] = p_\theta(u_\theta, v_\theta)$.

B. Feldkamp-Davis-Kress reconstruction

The Tuy conditions [4] are not satisfied in the cone-beam geometry with a circular orbit. Hence, only approximate direct reconstruction methods exist, such as the Feldkamp-Davis-Kress method [5], which is a direct extension of the fan-beam FBP to cone-beam data. Given a full-scan tomographic acquisition p, FDK reconstructs an image f_{FDK} as:

$$f_{\mathrm{FDK}} = \int_0^{2\pi} \frac{D^2}{s_\theta^2} \mathcal{B}_\theta \mathcal{D}[\widetilde{p}_\theta] \mathrm{d}\theta, \tag{3}$$

where $\mathcal{D}$ is the ramp filter, and:

$$\widetilde{p}_\theta(u, v) = \frac{1}{2} \cdot \frac{d}{D} \cdot \frac{D}{\sqrt{D^2 + u^2 + v^2}} \cdot p_\theta(u, v). \tag{4}$$

By design, FDK is equal to FBP when $z = 0$, yielding an exact reconstruction in the midplane. If the true image f is invariant along the z-axis, the reconstructed image f_{FDK} is exact [5]; otherwise, it deviates from f as the cone angle increases, yielding cone-beam artifacts.

In the following, we define $\{\Theta_k\}_{k=1\cdots K}$ as a subdivision of Θ. Then by linearity of the integral:

$$f_{\mathrm{FDK}} = \sum_{k=1}^{K} g_{\Theta_k}, \text{ where } g_{\Theta_k} = \int_{\Theta_k} \frac{D^2}{s_\theta^2} \mathcal{B}_\theta \mathcal{D}[\widetilde{p}_\theta] \mathrm{d}\theta. \tag{5}$$

A. Reshef (corresponding author: aymeric.reshef@ge.com) is with GE Healthcare, Buc, France, and LTCI, Télécom ParisTech, Université Paris-Saclay, Paris, France. C. Riddell and Y. Trousset are with GE Healthcare, Buc, France. S. Ladjal and I. Bloch are with LTCI, Télécom ParisTech, Université Paris-Saclay, France. This work was supported by the CIFRE grant No. 873/2014 from the French Association Nationale de la Recherche et de la Technologie (ANRT).

$\phi(t)$	$\mathcal{H}[\phi](t)$
$\mathcal{H}[\psi](t)$	$-\psi(t)$
$t\psi(t)$	$t\mathcal{H}[\psi](t) - \frac{1}{\pi}\int_{-\infty}^{+\infty}\psi(t')\mathrm{d}t'$
$\delta(t)$	$\frac{1}{\pi t}$
$\frac{1}{h_3 t+h_4}\psi\left(\frac{h_1 t+h_2}{h_3 t+h_4}\right)$, where $h_1h_4 - h_2h_3 = \pm 1$	$\frac{\mathrm{sgn}(h_1h_4-h_2h_3)}{h_3t+h_4}\mathcal{H}[\psi]\left(\frac{h_1t+h_2}{h_3t+h_4}\right)$

Table I: Useful Hilbert transforms to prove Eq. (7).

C. Proposed backprojection-filtration method

The proposed backprojection-filtration (BPF) formula is first derived in the fan-beam geometry. We rely on the decomposition of the ramp filter $\mathcal{D}$ into a spatial derivative operator and a Hilbert transform operator $\mathcal{H}$:

$$\mathcal{D}[\tilde{p}_\theta] = \frac{1}{2\pi}\mathcal{H}\left[\frac{\partial \tilde{p}_\theta}{\partial u}\right]. \tag{6}$$

When $\Theta_k = \{\theta\}$, we write $g_\theta = g_{\{\theta\}}$. Let $\alpha \in \Theta$ such that for any point $\boldsymbol{x}$ in the field of view, $\det\left(H_\theta^\alpha(\boldsymbol{x}\cdot\boldsymbol{\alpha})\right) \neq 0$. We define $\sigma_\theta^\alpha(\boldsymbol{x}) = \mathrm{sgn}\left(\det\left(H_\theta^\alpha(\boldsymbol{x}\cdot\boldsymbol{\alpha})\right)\right)$. The following holds:

$$g_\theta = \frac{\sigma_\theta^\alpha}{2\pi}\mathcal{H}_\alpha[b_\theta], \text{ where } b_\theta = \frac{D^2}{s_\theta^2}\mathcal{B}_\theta\left[\frac{\partial\tilde{p}_\theta}{\partial u}\right], \tag{7}$$

and $\mathcal{H}_\alpha$ applies the one-dimensional Hilbert transform to each line of the 2D plane that is colinear to $\boldsymbol{\alpha}^\perp$. We sketch the proof of Eq. (7). The homography matrix $H_\theta^\alpha(\boldsymbol{x}\cdot\boldsymbol{\alpha})$ is such that $\det\left(H_\theta^\alpha(\boldsymbol{x}\cdot\boldsymbol{\alpha})\right) \neq 0$, hence the determinant of the matrix $\left|\det H_\theta^\alpha(\boldsymbol{x}\cdot\boldsymbol{\alpha})\right|^{-1/2} H_\theta^\alpha(\boldsymbol{x}\cdot\boldsymbol{\alpha})$ is equal to σ_θ^α. We use the last row of Table I to obtain the intermediate result: $s_\theta g_\theta = \frac{\sigma_\theta^\alpha}{2\pi}\mathcal{H}_\alpha\left[\frac{D^2}{s_\theta}\mathcal{B}_\theta\left[\frac{\partial\tilde{p}_\theta}{\partial u}\right]\right]$. We then apply again $\mathcal{H}_\alpha$ to each side of this equality and observe that s_θ is an affine function of $\boldsymbol{x}$. Using the other properties of the Hilbert transform recalled in Table I, we obtain Eq. (7).

If $\Theta_k = [\theta_{k-1}, \theta_k]$ and $|\theta_k - \theta_{k-1}| < \pi - \gamma$, where γ is the fan angle, we can find a common admissible α value, denoted α_k, such that Eq. (7) holds for all $\theta \in \Theta_k$; hence:

$$g_{\Theta_k} = \frac{1}{2\pi}\int_{\Theta_k}\mathcal{H}_{\alpha_k}[b_\theta]\,\mathrm{d}\theta = \frac{1}{2\pi}\mathcal{H}_{\alpha_k}[b_{\Theta_k}], \tag{8}$$

where $b_{\Theta_k} = \int_{\Theta_k} b_\theta \mathrm{d}\theta$. We propose to reconstruct an image f_{BPF} as:

$$f_{\mathrm{BPF}} = \frac{1}{2\pi}\sum_{k=1}^{K}\mathcal{H}_{\alpha_k}[b_{\Theta_k}]. \tag{9}$$

As in FDK, the reconstruction formula from Eq. (9) is always exact in the midplane; it is exact everywhere when the true image f is invariant along the z-axis [5].

D. Implementation

The support of the backprojection over each angular subset Θ_k depends both on Θ_k and on the value of α_k. Provided that this support is large enough to compute all the backprojected lines colinear to $\boldsymbol{\alpha}_k^\perp$ and intersecting the image field of view (Fig. 1), the Hilbert transform can be computed directly in the Fourier domain using zero-padding and periodicity.

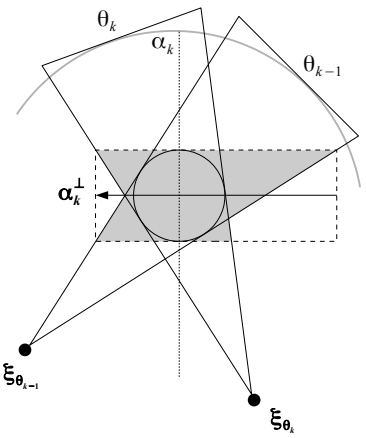

Fig. 1: Extended support (dashed rectangle) for filtering b_{Θ_k}. Lines colinear to $\boldsymbol{\alpha}_k^\perp$ (arrow) crossing the circular field of view (black circle) are all compactly supported (shaded area).

We divide Θ into frontal and lateral views. Frontal views correspond to $\Theta_{\mathrm{FRT}} = \left[\frac{\pi}{4}, \frac{3\pi}{4}\right] \cup \left[\frac{5\pi}{4}, \frac{7\pi}{4}\right]$. With $\alpha_{\mathrm{FRT}} = \frac{\pi}{2}$, image $b_{\Theta_{\mathrm{FRT}}}$ is filtered horizontally. Lateral views correspond to $\Theta_{\mathrm{LAT}} = \Theta \backslash \Theta_{\mathrm{FRT}}$. With $\alpha_{\mathrm{LAT}} = 0$, image $b_{\Theta_{\mathrm{LAT}}}$ is filtered vertically. Thus:

$$f_{\mathrm{BPF}} = \frac{1}{2\pi}\left(\mathcal{H}_{\frac{\pi}{2}}[b_{\Theta_{\mathrm{FRT}}}] + \mathcal{H}_0[b_{\Theta_{\mathrm{LAT}}}]\right). \tag{10}$$

III. Application to region-of-interest imaging

Following [3], we define a dual-rotation acquisition as follows. Let p_{T} be a set of truncated projections that finely sample the source-detector orbit. Projections p_{T} are complemented by additional un-truncated projections p_{F}. We do not intend to bring too much additional dose to the patient with the un-truncated projections, by either lowering the dose level per view or by reducing the number of views in p_{F}.

Since local operations are applied to projections p_{T} prior to backprojection, they correctly sample the unfiltered backprojected image b_{T} within the ROI, denoted Ω'. Outside the ROI, however, each backprojected point is observed over a limited angular range, which differs from one point to the other. We thus merge the ROI of b_{T} with the unfiltered backprojected image b_{F} obtained from p_{F}, yielding image $\mathcal{M}(b_{\mathrm{F}}, b_{\mathrm{T}})$ such that:

$$\mathcal{M}(b_{\mathrm{F}}, b_{\mathrm{T}}) = \begin{cases} \eta\cdot b_{\mathrm{F}} + (1-\eta)\cdot b_{\mathrm{T}} & \text{inside } \Omega'; \\ b_{\mathrm{F}} & \text{outside } \Omega'. \end{cases} \tag{11}$$

The function $\eta : \mathbb{R}^3 \to [0,1]$ is a continuous function that ensures a smooth transition from b_{T} to b_{F} at the boundaries of the ROI. The Fourier-based filtering step is then performed on the hybrid image $\mathcal{M}(b_{\mathrm{F}}, b_{\mathrm{T}})$. Using our BPF method, the merging step is performed separately for backprojections of the frontal views and of the lateral views.

IV. Simulations

All images were reconstructed on a $256 \times 256 \times 256$ grid with isotropic voxels of size 1.17 mm^3.

A. Full-volume reconstruction

A diagnostic CT scan of a head was forward-projected over an ideal circular orbit using $D = d = 1180$ mm. A total of 1440 projections sampling Θ was generated. The projections were reconstructed using FDK (yielding image f_{FDK}) and Eq. (10) (yielding image f_{BPF}). We computed the mean relative error (MRE) over a mask Ω_0, denoted $\Delta_{\Omega_0}(f_{\mathrm{BPF}}, f_{\mathrm{FDK}})$, using the formula:

$$\Delta_{\Omega}(f, f^*) = \frac{1}{\mathrm{Card}(\Omega)} \sum_{\boldsymbol{x}\in\Omega} \frac{|f(\boldsymbol{x}) - f^*(\boldsymbol{x})|}{|f^*(\boldsymbol{x})|} \qquad (12)$$

Mask Ω_0 was defined in order to keep only the voxels higher than -250 HU.

We repeated the experiment using modified projection data corresponding to $1.6 \cdot 10^6$ photons per ray emitted from the X-ray source, in order to check the stability of the method with respect to noise, yielding images $f_{\mathrm{FDK}}^{\mathrm{noisy}}$ and $f_{\mathrm{BPF}}^{\mathrm{noisy}}$.

B. Region-of-interest reconstruction

The truncated projections p_{T} were simulated by applying a digital transaxial truncation to the previous set of 1440 noisy projections, corresponding to a cylindrical, centered field of view Ω' whose edges cross the head skull. It is thus expected that empirical projection extrapolation methods would not perform as well. Such a reconstruction was computed using [6], yielding image $f_{\mathrm{FDK}}^{\mathrm{ROI}}$. For the un-truncated projections p_{F}, we simulated two configurations. In the first configuration, we simulated an acquisition of 1440 projections corresponding to 10^5 photons per ray emitted from the X-ray source, yielding image $f_{\mathrm{BPF}}^{\mathrm{ROI}(1)}$. In the second configuration, we simulated an acquisition of 90 projections corresponding to $1.6{\cdot}10^6$ photons per ray, yielding image $f_{\mathrm{BPF}}^{\mathrm{ROI}(2)}$. In both cases, the dose ratio between the un-truncated and the truncated acquisitions is fixed to 1/16. The merging step was performed using the following weighting function:

$$\eta(\boldsymbol{x}) = \frac{1}{2}\left(1 - \cos\left(\pi \cdot \frac{|\boldsymbol{x}| - r_{\Omega'}}{\Delta r}\right)\right), \qquad (13)$$

where $r_{\Omega'}$ denotes the radius of the cylindrical ROI Ω', and Δr is the transition zone radial width. In the following, Δr was arbitrarily set to 5 voxels. The MRE over the intersection set $\Omega = \Omega' \cap \Omega_0$ was computed with respect to the un-truncated FDK reconstruction $f_{\mathrm{FDK}}^{\mathrm{noisy}}$.

V. Results

A. Full-volume reconstruction

Noise-free reconstructed images are shown in Fig. 2. The images f_{FDK} and f_{BPF} are visually very similar. Both reconstructions are exact and identical in the fan-beam geometry of the midplane. However, f_{BPF} is more sensitive to the cone-beam incomplete sampling over a circular orbit (see the dark streaks near the temporal bones in the coronal and sagittal slices). Similar noise behavior occurs for both methods when reconstructing from noisy projections (images not shown). On average, the MRE inside Ω_0 is equal to 0.42% in the noise-free case and to 0.43% in the noisy case (Table II), the higher errors being located towards points with high cone angles.

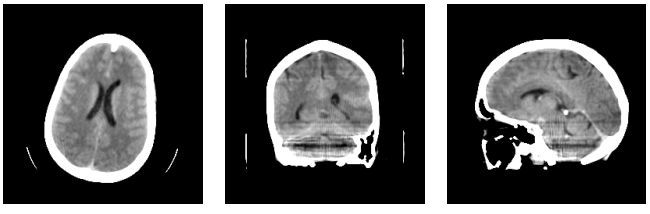

(a) f_{FDK} (axial) (b) f_{FDK} (coronal) (c) f_{FDK} (sagittal)

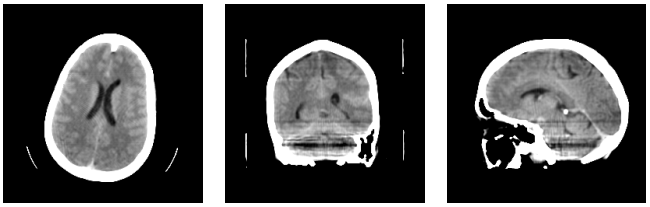

(d) f_{BPF} (axial) (e) f_{BPF} (coronal) (f) f_{BPF} (sagittal)

Fig. 2: Noise-free, full-volume reconstructions. Display window: [10 HU, 60 HU].

	Full-volume		ROI	
Ω	Ω_0		$\Omega' \cap \Omega_0$	
f	f_{BPF}	$f_{\mathrm{BPF}}^{\mathrm{noisy}}$	$f_{\mathrm{BPF}}^{\mathrm{ROI}(1)}$	$f_{\mathrm{BPF}}^{\mathrm{ROI}(2)}$
f^*	f_{FDK}	$f_{\mathrm{FDK}}^{\mathrm{noisy}}$	$f_{\mathrm{FDK}}^{\mathrm{noisy}}$	$f_{\mathrm{FDK}}^{\mathrm{noisy}}$
$\Delta_{\Omega}(f, f^*)$	0.42%	0.43%	0.44%	0.50%

Table II: Mean relative errors in region Ω.

B. Region-of-interest reconstruction

Results of ROI reconstruction are shown in Fig. 3. The first column shows the FDK reconstruction from the truncated projections only using empirical projection extrapolation. As expected, such extrapolation cannot perform well when highly contrasted structures such as bones lie at the edge of the field of view. The image $f_{\mathrm{FDK}}^{\mathrm{ROI}}$ suffers from a shift in gray values and from low-frequency non-uniformities that prevent from using a narrow window display.

Results from our reconstruction method are shown in the second and third columns of Fig. 3. Both configurations yield images that are visually similar to the reference FDK reconstruction $f_{\mathrm{FDK}}^{\mathrm{noisy}}$ (fourth column) inside the ROI Ω'. Outside the ROI, image $f_{\mathrm{BPF}}^{\mathrm{ROI}(1)}$ shows a very noisy reconstruction of the head, while image $f_{\mathrm{BPF}}^{\mathrm{ROI}(2)}$ shows streaks characteristic of angular subsampling. However, neither the high noise contained in p_{F} in the first configuration, nor the subsampling streaks of the second configuration propagate inside Ω'. The values of the MRE inside region $\Omega = \Omega' \cap \Omega_0$ with respect to $f_{\mathrm{FDK}}^{\mathrm{noisy}}$ remain below 1%, at 0.44% for $f_{\mathrm{BPF}}^{\mathrm{ROI}(1)}$ and 0.50% for $f_{\mathrm{BPF}}^{\mathrm{ROI}(2)}$ (Table II).

VI. Discussion

A new BPF formula was described for CBCT reconstruction with flat-panel detectors, that is exact in the fan-beam geometry and provides a different approximate reconstruction from FDK in the cone-beam geometry. It coincides with the parallel-beam Hilbert-transformed differentiated

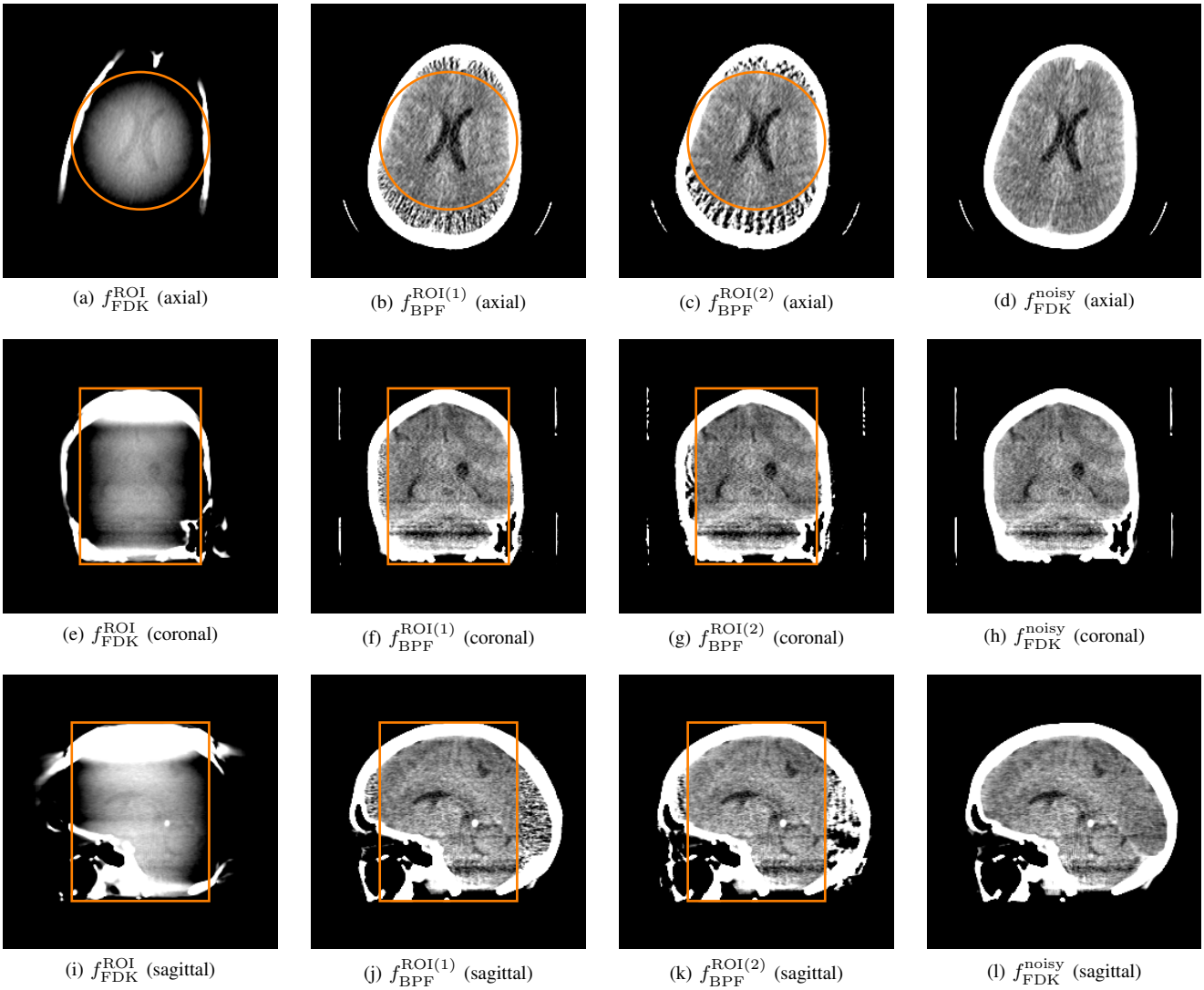

(a) $f_{\mathrm{FDK}}^{\mathrm{ROI}}$ (axial) (b) $f_{\mathrm{BPF}}^{\mathrm{ROI}(1)}$ (axial) (c) $f_{\mathrm{BPF}}^{\mathrm{ROI}(2)}$ (axial) (d) $f_{\mathrm{FDK}}^{\mathrm{noisy}}$ (axial)

(e) $f_{\mathrm{FDK}}^{\mathrm{ROI}}$ (coronal) (f) $f_{\mathrm{BPF}}^{\mathrm{ROI}(1)}$ (coronal) (g) $f_{\mathrm{BPF}}^{\mathrm{ROI}(2)}$ (coronal) (h) $f_{\mathrm{FDK}}^{\mathrm{noisy}}$ (coronal)

(i) $f_{\mathrm{FDK}}^{\mathrm{ROI}}$ (sagittal) (j) $f_{\mathrm{BPF}}^{\mathrm{ROI}(1)}$ (sagittal) (k) $f_{\mathrm{BPF}}^{\mathrm{ROI}(2)}$ (sagittal) (l) $f_{\mathrm{FDK}}^{\mathrm{noisy}}$ (sagittal)

Fig. 3: ROI reconstruction. The ROI Ω' is delineated in orange. Display windows: [-450 HU, -250 HU] (first column), [10 HU, 60 HU] (second to fourth columns).

backprojection method (DBP-HT) [1], when letting $(d, D) \to (+\infty, +\infty)$ and $K = 1$: in this case, image b_Θ becomes the parallel-beam DBP image, and filtration needs to be performed using finite Hilbert transform inversion. However, our approach differs from the fan-beam DBP-HT formula of [1]. In the fan-beam DBP-HT, the same DBP image is computed from fan-beam projections through a parallel-to-fan-beam change of variables, which requires a dense angular sampling. Instead, we propose to compute an alternative, intrinsically fan-beam DBP image, so that the whole backprojection step translates into a view-wise algorithm. Moreover, when $K > 1$, filtration is performed in the Fourier domain and does not require any finite Hilbert transform inversion. The method is thus expected to work as good as FDK with coarser angular sampling; it is also adapted to non-ideal circular geometries using calibrated projection matrices. As with FDK, the reconstructed images suffer from cone-beam artifacts, however, we anticipate faster iterative BPF reconstructions to reduce them [7]. Finally, excellent ROI reconstruction was obtained with only 6% of dose increase and flexible acquisition designs in terms of dose per view and angular sampling.

REFERENCES

[1] F. Noo, R. Clackdoyle, and J. D. Pack, "A two-step Hilbert transform method for 2D image reconstruction," *Physics in Medicine and Biology*, vol. 49, no. 17, p. 3903, 2004.

[2] H. Kudo, M. Courdurier, F. Noo, and M. Defrise, "Tiny a priori knowledge solves the interior problem in computed tomography," *Physics in Medicine and Biology*, vol. 53, no. 9, p. 2207, 2008.

[3] A. Reshef, C. Riddell, Y. Trousset, S. Ladjal, and I. Bloch, "Dual-rotation C-arm cone-beam computed tomography to increase low-contrast detection," *Medical Physics*, vol. 44, no. 9, pp. e164–e173, 2017.

[4] H. K. Tuy, "An inversion formula for cone-beam reconstruction," *SIAM Journal on Applied Mathematics*, vol. 43, no. 3, pp. 546–552, 1983.

[5] L. Feldkamp, L. Davis, and J. Kress, "Practical cone-beam algorithm," *JOSA A*, vol. 1, no. 6, pp. 612–619, 1984.

[6] J. Hsieh, R. H. Armstrong, P. J. Arduini, and R. F. Senzig, "Methods and apparatus for truncation compensation," 2004, US Patent 6,810,102.

[7] H. Langet, C. Riddell, A. Reshef, Y. Trousset, A. Tenenhaus, E. Lahalle, G. Fleury, and N. Paragios, "Compressed-sensing-based content-driven hierarchical reconstruction: Theory and application to C-arm cone-beam tomography," *Medical Physics*, vol. 42, no. 9, pp. 5222–5237, 2015.